Soils and Foundations 2013;53(5):774–783

The Japanese Geotechnical Society

Soils and Foundations

www.sciencedirect.com
journal homepage: www.elsevier.com/locate/sandf

Development of high-pressure low-temperature plane strain testing apparatus for methane hydrate-bearing sand

Jun Yoneda[a,*,1], Masayuki Hyodo[b], Norimasa Yoshimoto[b], Yukio Nakata[b], Akira Kato[b]

[a]*The National Institute of Advanced Industrial Science and Technology (AIST), Japan*
[b]*Graduate School of Science and Engineering, Yamaguchi University, Japan*

Received 15 July 2012; received in revised form 25 June 2013; accepted 20 July 2013
Available online 27 September 2013

Abstract

A high-pressure low-temperature plane strain testing apparatus was developed for visualizing the deformation of methane hydrate-bearing sand due to methane hydrate production. Using this testing apparatus, plane strain compression tests were performed on pure Toyoura sand and methane hydrate-bearing sand with localized deformation measurements. From the results, it was observed that the methane hydrate-free specimens, despite their relatively high density, showed changes in compressive volume. Marked increases in the initial stiffness and strength of the methane hydrate-bearing sand were observed (methane hydrate saturation of $S_{MH}=60\%$). Moreover, the volumetric strain changed from compressive to dilative. For the specimens with methane hydrate, a dilative behavior above $S_{MH}=0\%$ was observed. An image analysis showed that the shear bands of the methane hydrate-bearing sand were thinner and steeper than those of the host sand. In addition, the dilative volumetric strain in the shear band increased markedly when methane hydrate existed in the pore spaces.

Keywords: Methane hydrate; Deformation; Compression; Plane strain; Depressurization; Localization

1. Introduction

Recent investigations have shown that methane hydrate (hereafter referred to as MH) is a potential future energy resource. Both thermal recovery methods and depressurization methods have been suggested and developed for extracting methane gas from MH-bearing sediment reservoirs in deep ocean floors, for example, the *Nankai Trough* (Yamamoto, 2009; Fujii et al., 2008; Nagakubo, 2009). Using both methods, MH in the ground is dissociated to release methane gas. Hydrates in the pore spaces of sand can be classified into three types: pore-filling, load-bearing and cementing (Waite et al., 2009). These three types of hydrate-bearing sediment can be prepared in the laboratory by three different methods, namely, using hydrate grains and ice seeding (Hyodo et al., 2005; Ebinuma et al., 2005), applying partial water saturation (Kneafsey et al., 2005; Waite et al., 2004), and employing dissolved gas (Katsuki et al., 2006; Tohidi et al., 2001). In the case of pore-filling, the hydrate exists in the pore spaces with no bridging between soil particles and affects the pore fluid bulk stiffness and fluid conduction properties (Helgerud et al., 1999). In the case of load-bearing, the hydrate bridges the soil particles and confers the mechanical stability to the granular skeleton by becoming part of the load-bearing framework. Pore-filling

*Corresponding author. Tel.: +81 29 861 8306; fax: +81 29 861 8765.
E-mail address: jun.yoneda@aist.go.jp (J. Yoneda).
[1]National Institute of Advanced Industrial Science and Technology, Japan.
Peer review under responsibility of The Japanese Geotechnical Society.

Production and hosting by Elsevier

0038-0806
http://dx.doi.org/10.1016/j.sandf.2013.08.014

hydrate naturally becomes of the load-bearing type when the pore space hydrate saturation exceeds S_h=25–40% (Yun et al., 2005, 2007). In this case, shear stiffness and peak strength increase with increasing hydrate saturation and significant dilative behavior is observed when hydrate saturation S_h exceeds 40% (Yun et al., 2005, 2007; Masui et al., 2005). In the third case, cementing, the hydrate cements the intergranular contacts. If the host sand is dense, even a small amount of hydrate can markedly increase sediment shear and bulk stiffness by bonding the adjacent grains together. For this type of MH-bearing sediment, experiments under various conditions have shown that its mechanical properties are dependent on hydrate saturation, confining pressure, soil density, particle distribution, temperature, and water pressure (Berge et al., 1999; Yun et al., 2005, 2007; Hyodo et al., 2007, 2008a, 2008b; Yoneda et al., 2010; Miyazaki et al., 2010, 2011). Researchers have discussed the obtained relationships of dilatancy with mobilized shear strength and stiffness; in particular, Yun et al. (2005) and Waite et al. (2009) proposed a possible micro-mechanical model for hydrate-bearing sediment. Then, several constitutive models (e.g., Hyodo et al., 2008a, 2008b; Uchida et al., 2012) have been proposed on the basis of their idea, and seabed deformation due to MH exploitation was predicted (Kimoto et al., 2007; Klar et al., 2010; Yoneda et al., 2011).

For any soil sediments consisting of discrete particles and associated voids, a mechanical examination of the localized shear band deformation is significant for evaluating and modeling the mechanical properties of these sediments from a micro-mechanical viewpoint (e.g., Newland and Allely, 1957; Rowe, 1962). Different types of elemental tests, for example, plane strain and box shear tests, have been performed to investigate the angle (Tatsuoka et al., 1986; Khalid and Stein, 2000), the width and the mechanism of the generation of shear bands (Tatsuoka et al., 1990; Ueno et al., 2000; Ikeda et al., 2003) under low and medium confining pressures. In addition, model tests such as bearing capacity tests (White et al., 2003), have been carried out to clarify the micro-mechanical deformation properties of foundations. Recently, research studies using X-ray CT have been widely used, and the behavior of soil particles on shearing is becoming clear (Otani et al., 2000; Hall et al., 2010; Ando et al., 2011; Higo et al., 2011, 2013). Thus far, tests must be performed at high pore water pressures and low temperatures with high confining pressures to examine the MH reservoirs. Hence, failure patterns of MH-bearing sand have not yet been observed. The realization of deformation is significant from the gas production point of view, because there are concerns about gas leakage and/or channel formation in alignment with localized deformation like shear bands. In the present study, a plane strain testing apparatus that can simulate the predicted high pore water pressure, low temperature, and confining pressure corresponding to those existing in situ, and that can be applied in compression shear tests. is developed to investigate the effect of hydrate bearing under high confining pressure on the constitutive behavior of sand materials. In addition, the localized deformation of MH-bearing sand was observed visually.

2. Plane strain testing apparatus

A high-pressure low-temperature plane strain testing apparatus has been developed to examine and visualize the deformation of MH-bearing sand. Fig. 1(a) shows an overview of the temperature-controlled room where the equipment, shown in Fig. 1(b) and (c), was installed to generate MH at a given temperature.

The experiments were controlled using a PC set up outside the room. Fig. 2 shows a schematic diagram of the apparatus. A detailed description of each part shown in this figure is presented below.

(a) *Test specimen*
The sample was 80 mm (length) × 60 mm (width) × 160 mm (height).

(b) *Pressure cell*
The pressure cell had thick acrylic observation windows (c) installed in the front and the back of the specimen through which pictures could be taken.

(c) *Observation window*
The thickness of the observation window was 70 mm. The window is capable of tightening a confining plate. The observing direction is the same as that of applied intermediate stress σ_2 in the plane strain.

(d) *Confining plate*
A confining plate was used to maintain plane strain conditions during the testing with an acryl block 70 mm in thickness. LEDs on the left, the right, the top, the center,

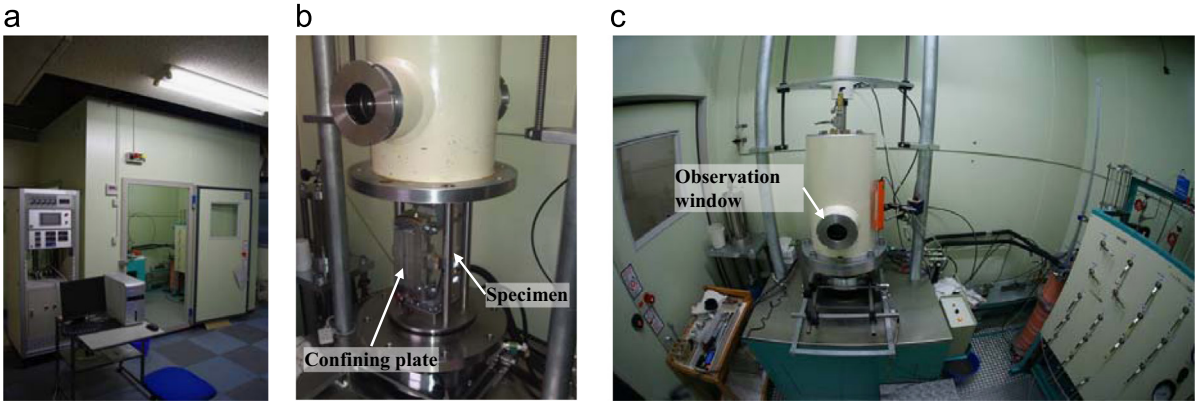

Fig. 1. (a) Exterior view of refrigeration room; (b) setting of specimen; (c) exterior view of homeothermic high-pressure plane strain device.

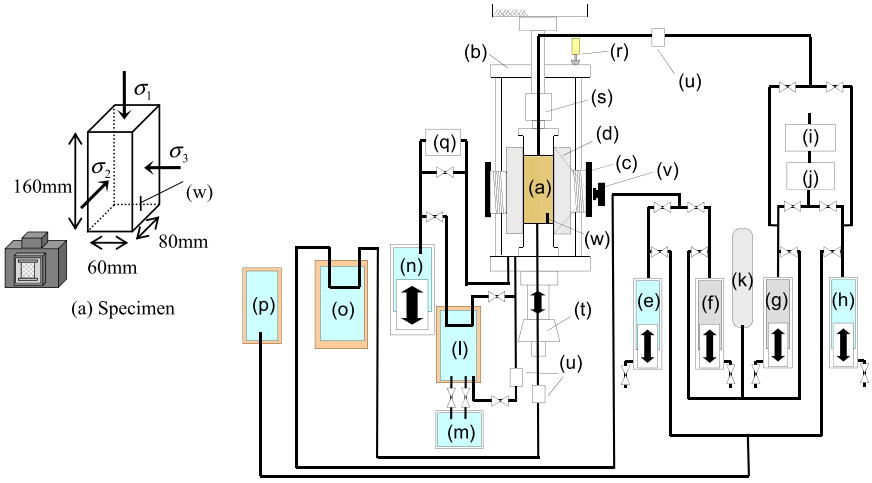

Fig. 2. Schematic diagram of testing apparatus. (a) Specimen; (b) pressure cell; (c) observation window; (d) confining plate; (e) lower syringe pump for water; (f) lower syringe pump for gas; (g) upper syringe pump for gas; (h) upper syringe pump for water; (i) mass flow meter; (j) separation tank; (k) methane gas bottle; (l) cell liquid tank; (m) heat control tank; (n) confining pressure amplifier; (o) heating tank; (p) heating tank; (q) cell liquid pump; (r) displacement transducer; (s) load cell; (t) loading equipment; (u) pressure gage; (v) camera; and (w) thermocouple.

and the bottom of the confining plate facilitated taking photos of the specimen using a remote-control camera with a timer.

(e), (f), (g) and (h) *Syringe pumps for water and gas*

Two syringe pumps were connected to the top and the bottom of the specimen, which not only controlled the pressure of the water and the methane gas, but also measured the changes in specimen volume.

(i) *Gas mass flow meter*

A gas mass flow meter was used to measure the amount of methane gas after the tests. To calculate the MH saturation ratio, a mass flow meter for the gas was installed in the pipe. The gas that passed through the device was measured as mass flow (in g/min) independent of temperature and pressure and shown as flow volume (in mL/min) standardized at 20 °C and −1 atm. In addition, the amount of gas could be measured by calculation.

(j) *Separation tank*

This device separated the gas from the water in order to measure the methane gas.

(k) *Methane gas bottle*

Methane gas flowed to the pipe from this bottle and was used to fill the inside of the syringe pumps to generate MH.

(l) *Cell liquid tank*

This device consisted of a system for adjusting the temperature from 0 °C to +30 °C within the pressure cell by circulating the cell fluid in the plane strain testing device from an external temperature-controlled water tank. The temperature in the tank could be controlled within a range of ±0.1 °C.

(m) *Heat control tank*

This device consisted of a system for adjusting the temperature from 0 °C to +50 °C within the cell liquid tank. The temperature in the tank could be controlled within the range of ±0.1 °C.

(n) *Confining pressure amplifier*

Cell pressures of up to 20 MPa, controllable within the range of ±0.1 MPa, were supplied by oil pressure.

(o), (p) *Heating tank*

This device consisted of a system for adjusting the temperature from 0 °C to +50 °C within the syringe pump. The temperature of the tank could be controlled within the range of ±0.1 °C.

(q) *Cell liquid pump*

The cell liquid pump circulates water into the pressure cell.

(r) *Displacement transducer*

This device is for measuring the vertical displacement of the specimen.

(s) *Load cell*

To eliminate the effect of piston friction, a cylindrical loading cell, which is not affected by temperature or pressure, was set up in the cell. The maximum permissible load was 200 kN, and it was possible to measure it with an accuracy of 1/1000 for the full-scale load.

(t) *Loading equipment*

To apply high compression stress, a piston designed to resist up to 200 kN was installed; loading was performed via a pulse-controlled method using a stepping motor.

(u) *Pressure gage*

The pressure gage measures the pore pressure and the cell pressure up to 20 MPa.

(v) *Camera & lens*

A 25-million-pixel digital single-lens reflex camera was used. A fisheye lens (15 mm F2.8) was used for observing the whole specimen from the window.

(w) *Thermocouple*

A thermometer was installed inside the specimen, and the temperature in the triaxial room was measured. The temperature of the cell was controlled on the basis of the value indicated by the thermometer.

3. Generation of MH and experimental procedure

MH-bearing sand was artificially produced on the basis of the observation that MH existed within the pores of the sediment bridging the particles of the undisturbed core samples taken from the *Nankai* Trough (Suzuki et al., 2006). Toyoura sand was chosen as the host sand with a mean particle size of 0.162 mm. A given amount of water, calculated from the MH saturation target, was mixed with sand whose volume was determined to correspond to the target density. Moist soil was arranged in 12 layers in a silicon membrane and each layer was molded by compaction using a tamper 40 times.

After forming the specimen, it was subjected to a series of processes under specified temperatures and pressures, as depicted in Fig. 3. Firstly, the specimen was set up inside the pressure cell (a) and subjected to 0.2 MPa of confining pressure for self-withstanding. Then, the pore pressure and the confining pressure were gradually increased to 5 MPa and 5.2 MPa, respectively, while methane was being injected into the specimen and the specimen was kept at the temperature and pressure where stable MH could exist (b). At this stage, the gas pressure was increased gradually with time so that the specimen's moisture content would not become non-uniform as a result of the pressurized injection. By keeping the gas pressure constant in the connection between the specimen and the syringe pump, and by observing the amount of gas flowing at various times, the transformation of water within the pores into the hydrate was judged to be complete when there were no marked changes in the amount of gas. After the hydrate was generated for 3 days, the gas in the pipe was then substituted with water under constant pressure, and water was allowed to infiltrate the specimen for 2 days. Then, pore-water pressure was applied (c) and the temperature was adjusted to follow the prescribed test conditions (d). While keeping the pressure constant, consolidation was carried out until the specified mean effective stress was reached. After a compression shear test, pore pressure was released, the temperature of the specimen increased, and MH dissociated. The amount of gas was measured using the gas flow meter shown in Fig. 1(b). The amount of gas measured allowed the estimation of the MH saturation, assuming the density of MH to be 0.913 g/cm^3 (Sloan, 1998).

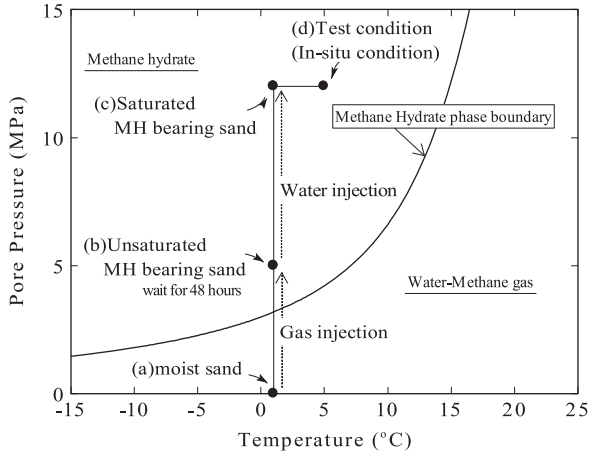

Fig. 3. Paths of pressure and temperature followed in producing MH-bearing sand.

4. Plane strain compression tests for MH-bearing sand

Specimens were prepared without MH (pure Toyoura sand/MH saturation of $S_{MH}=0\%$) and with MH (MH saturation of $S_{MH}=60\%$) with an effective confining pressure of 3.5 MPa and a porosity of 40%. In previous results (Masui et al., 2005; Hyodo et al., 2007, 2013; Miyazaki et al., 2011) of triaxial tests on Toyoura sand containing a synthetic gas hydrate, it has been confirmed that an increase in hydrate saturation tends to stimulate strain softening. Therefore, specimens were prepared to generate high MH saturation in this research. Shearing was conducted at a strain rate of 0.1%/min. Fig. 4 shows the deviator stress, axial strain, and volumetric strain relations. From the figure, it is observed that both cases, with and without MH specimens, show an initially compressive volume change and strain softening after hardening. Volumetric strain without MH specimens increased all along, notwithstanding the high relative density. This behavior might be due to the effect of grain crushing because of the high confining pressure (Miura et al., 1977). Marked increases in the initial stiffness and strength are observed in the case with MH. Changes in volumetric strain from compressive to dilative are seen for the specimen with $S_{MH}=60\%$ instead of compressive behavior only for the specimen with $S_{MH}=0\%$. This is believed to be due to the hardening action induced by MH on the sand particles.

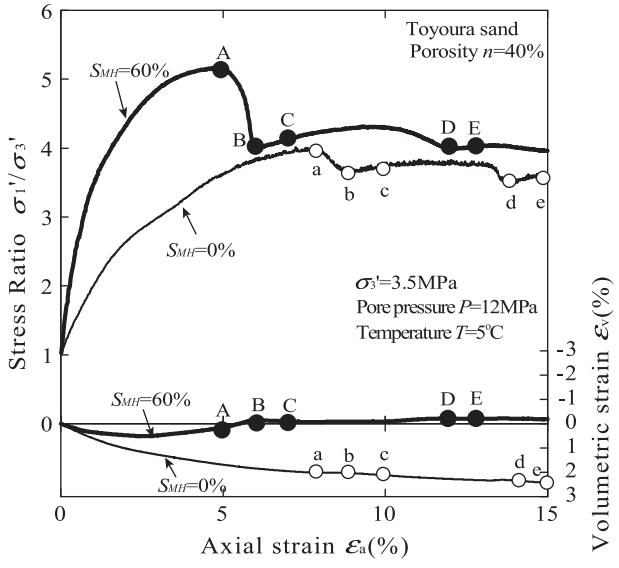

Fig. 4. Stress strain curves for host sand and MH-bearing sand.

5. Localized deformation

Several analytical methods have already been proposed for evaluating localized deformation. For example, (1) tracking intersections on the sealing sleeve (Tatsuoka et al., 1990), (2) gamma-rays (Desrues et al., 1985), (3) stereophotogrametry (Desrues and Viggiani, 2004), (4) X-ray computed tomography (Desrues et al., 1996; Hall et al., 2010), and (5) Particle image

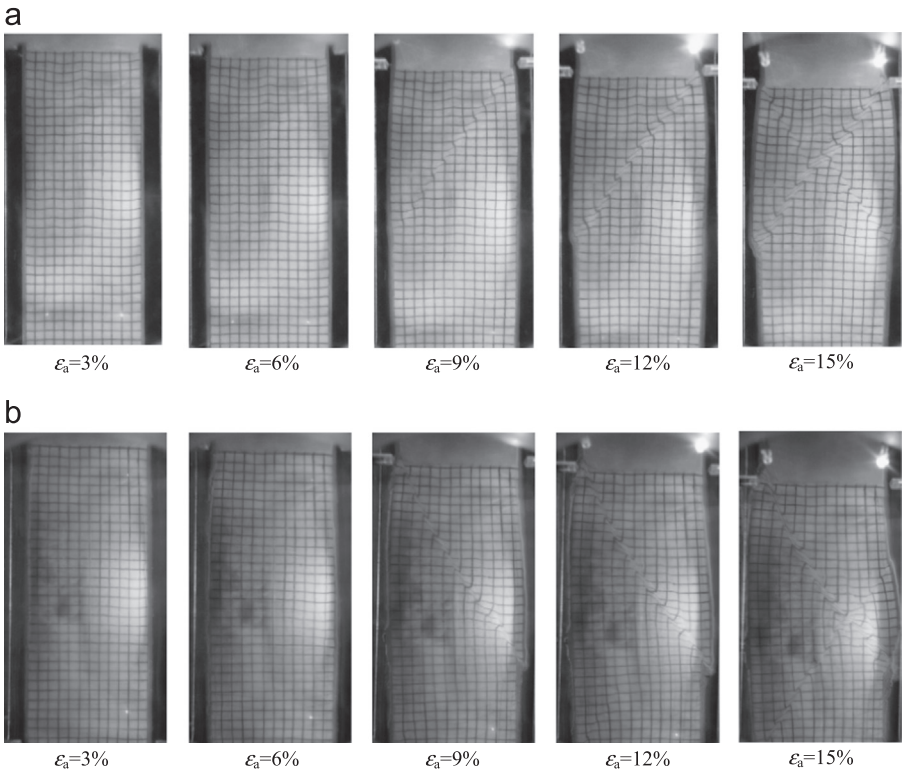

Fig. 5. Photographs during compression tests: (a) S_{MH}=0% and (b) S_{MH}=60%.

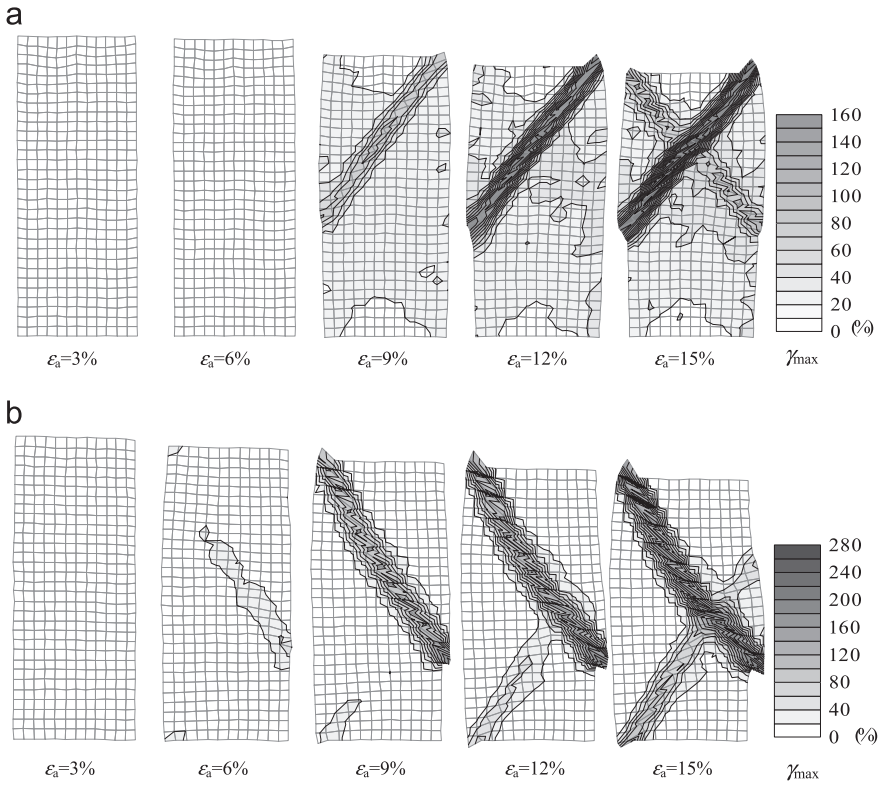

Fig. 6. Cumulative maximum shear strains during compression tests: (a) S_{MH}=0% and (b) S_{MH}=60%.

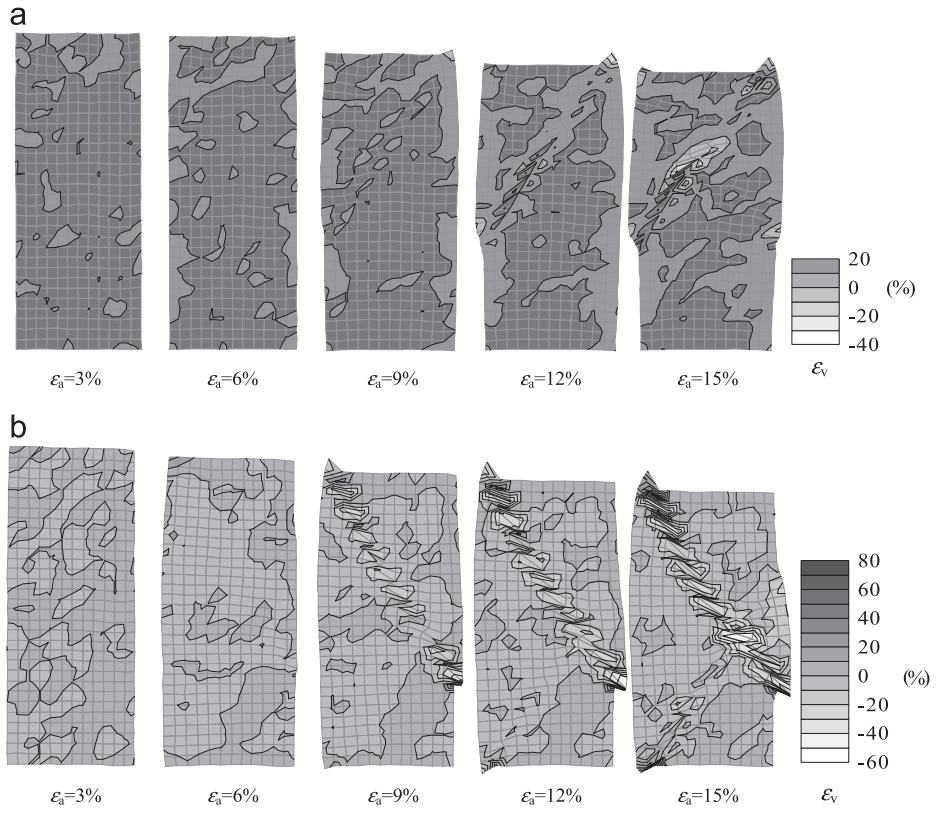

Fig. 7. Volumetric strains during compression tests: (a) S_{MH}=0% and (b) S_{MH}=60%.

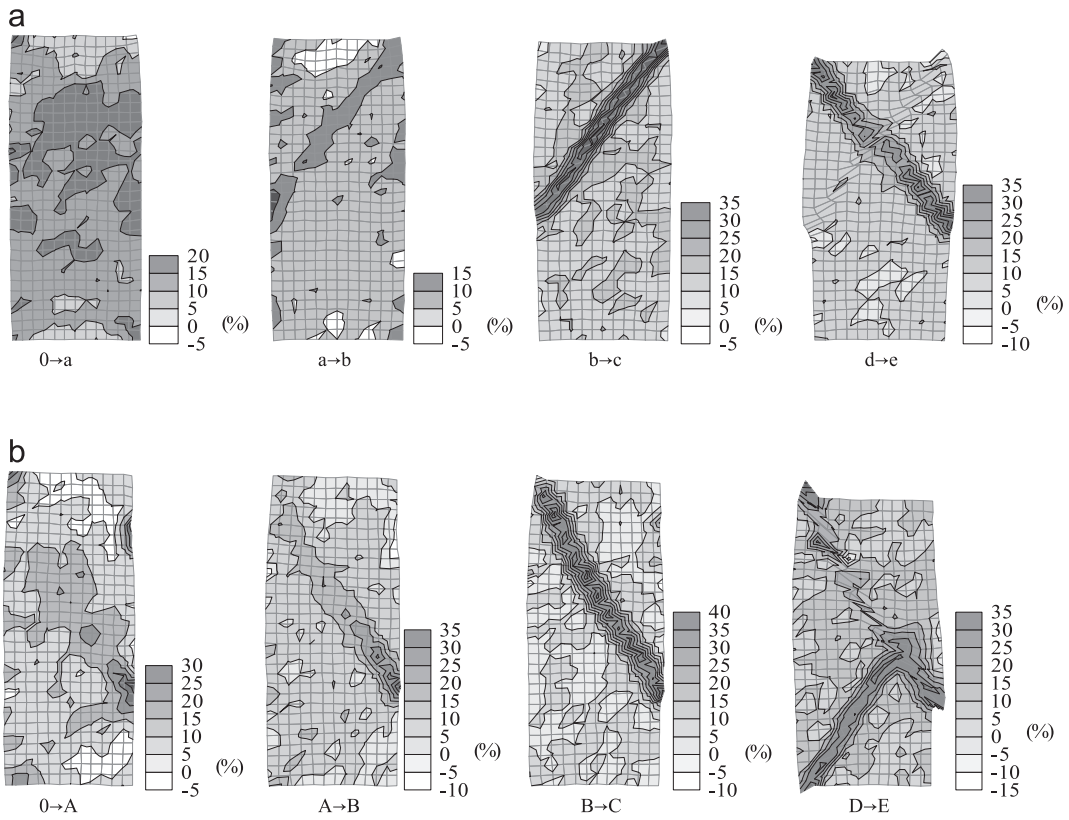

Fig. 8. Incremental maximum shear strains during compression tests: (a) S_{MH}=0% and (b) S_{MH}=60%.

velocimetry (White et al., 2003). Here, the simplest method, (1), is used. Digital photos were taken at each axial strain level. Geometric correction was performed on the photographs to cancel the distortion of the lens by polynomial reduction methods. Localized shear strain and volumetric strain were monitored during the compression tests. Figs. 6–8 show the contours of the maximum shear strain and the volumetric strain at each strain level, seen on the sigma-2 plane of each specimen, defined for the initial dimensions of each specimen. These were constructed from the strain increments defined for the elements on the lateral plane, as shown in Fig. 5. The strain increments were obtained from the incremental displacements measured at four nodes of each element, assuming linear changes in the strain increments for each element. Strain was calculated from the deformation gradient tensor and the Lagrange strain tensor defined by the shape function matrix and the deformation matrix of the four nodes as with finite element method analyses. The contours were depicted on the basis of this strain. The incremental displacement was determined by measuring the coordinates of every node of the grid, which was provided by the distinct center of the intersection point.

Fig. 5 shows the (a) $S_{MH}=0\%$ (pure sand) and (b) $S_{MH}=60\%$ specimens during compression testing at various strains. At (a) $S_{MH}=0\%$, two shear bands were observed. These shear bands appeared when strain softening occurred, as indicated in Fig. 4. Thus, it seems that the stresses are concentrated inside the shear band. Next, at (b) $S_{MH}=60\%$, two shear bands were also observed. These shear bands appeared during strain softening in Fig. 4 in the same manner as those observed in pure sand. The distribution of the cumulative maximum shear strain γ_{max} for $S_{MH}=0\%$ and 60% at various axial strains is shown in Fig. 6. The shear band of $S_{MH}=60\%$ appeared earlier than that of $S_{MH}=0\%$. The cumulative maximum shear strain γ_{max} of $S_{MH}=0\%$ is 160% and that of $S_{MH}=60\%$ is 280%. In addition, the strain field of $S_{MH}=0\%$ spread along the shear band wider than that of $S_{MH}=60\%$. The distribution of cumulative volumetric strain ε_v for each strain is shown in Fig. 7. Here, compression is defined as both positive and expansion-negative. At both (a) $S_{MH}=0\%$ (pure sand) and (b) $S_{MH}=60\%$, the shear bands observed in Fig. 5 dilated with increasing axial strain. At a given strain level, the volumetric strain of (b) $S_{MH}=60\%$ is greater than that of (a) $S_{MH}=0\%$. The distribution of the incremental maximum shear strain γ_{max}, for each section from a/A to e/E in Fig. 4, is shown in Fig. 8. In both cases with and without the MH specimen, shear bands were not observed in 0 to a/A sections. The first shear band initiated in the sections form the a/A to b/B overall axial strains followed by softening in the nominal stress response. Shear strain increased in b/B to c/C. The second shear band was initiated in d/D to e/E after additional shearing along the first shear band. Shearing then continued along the two bands until the completion of the test.

The thicknesses of the shear bands, i.e., (a)=1.8 mm and (b)=1.0 mm, were measured from Fig. 9. The shear band thickness was measured from the parallel lines drawn where the curvature of the grid lines was at a maximum. The thickness of the shear band at low confining pressures was measured by Tatsuoka et al., 1986 to be about 20 times the mean particle size. This is about 3.2 mm for Toyoura sand with a mean particle size. However, the thickness of the shear band

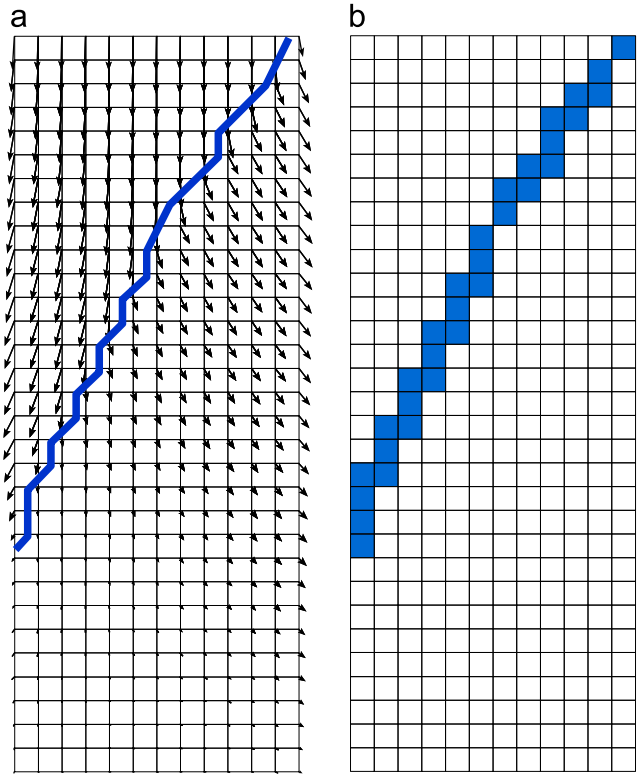

Fig. 10. Assumed shear band. (a) Center of shear band and (b) assumed shear band.

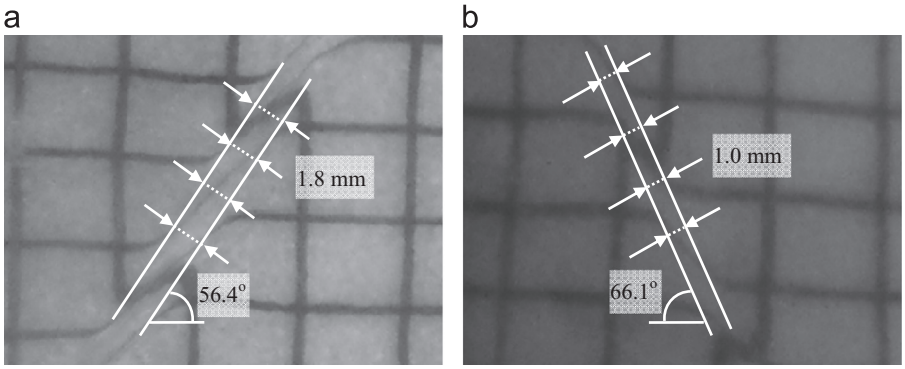

Fig. 9. Thicknesses and failure angles of shear bands. (a) $S_{MH}=0\%$ and (b) $S_{MH}=60\%$.

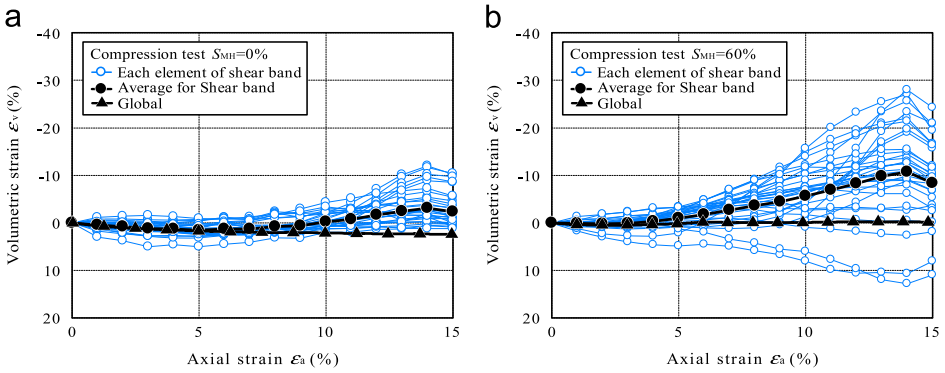

Fig. 11. Volumetric strain of each element in shear band with global volumetric strain. (a) S_{MH}=0% and (b) S_{MH}=60%.

in this study was about 10 times the mean particle size. This is due to the high confining pressure. A decrease in the thickness of the shear band with an increase in the confining pressure was observed in the plane strain compression tests under low confining pressures (Yoshida et al., 1994; Pradhan, 1997). Moreover, Tejchman et al. (2012) reported that the thickness of the shear band decreases with grain crushing because of an increase in confining pressure, as determined by the FE analysis. Toyoura sand might be crushed under high confining pressures in this study. In addition, the thickness of the shear band of (b) S_{MH}=60% is thinner than that of (a) S_{MH}=0% due to the MH cementation. Next, to evaluate the volumetric strain quantitatively, the shear band was extracted at each axial strain level. The shear band that appears in the specimen is not completely or necessarily a straight line. Therefore, a process for extracting the element of a shear band is proposed (Kikkawa et al., 2007). Fig. 10 shows the process for establishing elements containing a shear band. In Fig. 10(a), the centers of the shear band are extracted by connecting the points where the displacement increment vector diverged right and left from the perpendicular direction. Next, the shear band was described in Fig. 10(b) by the elements through which the line passed. Fig. 11(a) and (b) shows the volumetric strain for each element at each axial strain level during the compression tests. In the case of a hydrate saturation of S_{MH}=0%, each shear band element shows dilative behavior, although the global volumetric strain was kept compressive. It was observed that the average volumetric strain of the shear band elements decreased from an axial strain of 8%. Next, for a hydrate saturation of S_{MH}=60%, most of the shear band elements dilated markedly, although some elements showed compressive behavior. The average volumetric strain of the shear band elements was dilative from an axial strain of 6%.

6. Conclusions

Plane strain compression shear tests, with the measurement of localized deformation, were performed using a high-pressure low-temperature plane strain testing apparatus. From the results, it was observed that the specimens showed a change in the compressive volume at a confining pressure of 3.5 MPa. Moreover, for MH-bearing sand, marked increases in the initial stiffness and strength were observed. The volumetric strain changed from compressive to dilative, and for specimens with S_{MH}=60%, a significant dilative behavior was observed. Using an image analysis, the shear band of the MH-bearing sand was found to be thinner than that of the host sand. In addition, the dilative volumetric strain in the shear band increased markedly when MH existed in the pore spaces.

There are still many characteristics that remain unclear, such as the dependence of the degree of MH saturation and variations in the effective confining pressure, shear strain rate, and stress-anisotropy. This high-pressure low-temperature plane strain testing equipment will contribute to investigations of the shearing mechanism of MH-bearing sand. Such systematic experiments are expected to further the understanding of the general and local mechanical properties of MH-bearing sand.

Acknowledgments

This work was supported by KAKENHI 20246080 for which the authors are grateful. Thanks are also due to our sponsors and partners. We appreciate the insightful discussions with and the support of the members of the Research Consortium for Methane Hydrate Resources in Japan (MH21 Research Consortium) in Japan's Methane Hydrate R&D Program of the Ministry of Economy, Trade and Industry (METI). Thanks are also given to Professor Emeritus Adrian Hyde of the University of Sheffield who forsook his alpine retirement idyll to edit this paper.

References

Ando, E., Hall, A.S., Desrues, J., Besuelle, P., 2011. Grain-scale experimental investigation of localised deformation in sand: a discrete particle tracking approach. Acta Geotechnica 7 (1), 1–13. http://dx.doi.org/10.1007/s11440-0151-6.

Berge, L.I., Jacobsen, K.A., Solstad, A., 1999. Measured acoustic wave velocities of R11(CCl 3F) hydrate samples with and without sand as a function of hydrate concentration. Journal of Geophysical Research 104, 15,415–15,424. http://dx.doi.org/10.1029/1999JB900098.

Desrues, J., Lanier, J., Stutz, P., 1985. Localization of the deformation in tests on sand sample. Engineering Fracture Mechanics 21, 909–921.

Desrues, J., Chambon, R., Mokni, M., Mazerolle, F., 1996. Void ratio evolution inside shear bands in triaxial sand specimens studied by computed tomography. Geotechnique 46 (3), 527–546.

Desrues, J., Viggiani, G., 2004. Strain localization in sand: an overview of the experimental results obtained in Grenoble using stereophotogrammetry. International Journal for Numerical and Analytical Methods in Geomechanics 28 (4), 279–321.

Ebinuma, T., Kamata, Y., Minagawa, H., Ohmura, R., Nagao, J., Narita, H., 2005. Mechanical properties of sandy sediment containing methane hydrate. In: Proceedings of the Fifth International Conference on Gas Hydrates, Tapir Acad., Trondheim, Norway, pp. 958–961.

Fujii, T., et al., 2008. Resource Assessment of Methane Hydrate in the Eastern Nankai Trough. In: Proceedings of 2008 Offshore Technology Conference, Japan, OTC19310.

Hall, S.A., Bornert, M., Desrues, J., Pannier, Y., Lenoir, N., Viggiani, G., Bésuelle, P., 2010. Discrete and continuum analysis of localised deformation in sand using X-ray micro CT and volumetric digital image correlation. Géotechnique 60 (5), 315–322.

Helgerud, M.B., Dvorkin, J., Nur, A., Sakai, A., Collett, T., 1999. Elastic-wave velocity in marine sediments with gas hydrates: effective medium modeling. Geophysical Research Letters 26, 2021–2024. http://dx.doi.org/10.1029/1999GL900421.

Higo, Y., Oka, F., Kimoto, S., 2011. Study of strain localization and microstructural changes in partially saturated sand during triaxial tests using microfocus X-ray CT. Soils and Foundations 51 (1), 95–111.

Higo, Y., Oka, F., Sato, T., Matsuhima, Y., Kimoto, S., 2013. Investigation of localized deformation in partially saturated sand under triaxial compression using microfocus X-ray CT with digital image correlation. Soils and Foundations 53 (2), 181–198.

Hyodo, M., Nakata, Y., Yoshimoto, N., Ebinuma, T., 2005. Basic research on the mechanical behavior of methane hydrate–sediments mixture. Soils and Foundations 45 (1), 75–85.

Hyodo, M., Nakata, Y., Yoshimoto, N., Yoneda, J., 2007. Mechanical behavior of methane hydrate-supported sand. In: Proceedings of International Symposium on Geotechnical Engineering, Ground Improvement and Geosynthethics for Human Security and Environmental Preservation, pp. 195–208.

Hyodo, M., Nakata, Y., Yoshimoto, N., Yoneda, J., 2008a. Shear strength of methane hydrate bearing sand and its deformation during dissociation of methane hydrate. In: Proceedings of the 4th International Symposium on Deformation Characteristics of Geomaterials, pp. 549–556.

Hyodo, M., Nakata, Y., Orense, R., Yoshimoto, N., Yoneda, J., 2008b. Elastoplastic constitutive equation for methane hydrate-supported sand in deep seabed. In: Proceedings of 14th International Symposium on Plasticity, pp. 349–351.

Hyodo, M., Yoneda, J., Yoshimoto, N., Nakata, Y., 2013. Mechanical and dissociation properties of methane hydrate-bearing sand in deep seabed. Soils and Foundations 53 (2), 299–314 (doi: 10.1016/j.sandf.2013.02.010).

Ikeda, K., Ichimura, T., Takamura, H., Sudo, Y., 2003. Image processing of deformation behavior of plane strain compression specimens based on bifurcation mechanism. Journal of JSCE (III): Geotechnical Engineering 757 (66), 167–176 (in Japanese).

Katsuki, D., Ohmura, R., Ebinuma, T., Narita, H., 2006. Formation, growth and ageing of clathrate hydrate crystals in a porous medium. Philosophical Magazine 86, 1753–1761. http://dx.doi.org/10.1080/14786430500509062.

Khalid, A., Stein, S., 2000. Shear band formation in plane strain experiments of sand. Journal of Geotechnical and Geoenvironmental Engineering 126 (6), 495–503.

Kikkawa, N., Nakata, Y., Hyodo, M., Murata, H., Nishio, S., 2007. Analysis of shear band on sandy soil in triaxial test using image processing techniques. Journal of JSCE(III): Geotechnical Engineering 63 (1), 59–71 (in Japanese).

Kimoto, S., Oka, F., Fushita, T., Fujiwaki, M., 2007. A chemo-thermo-mechanically coupled numerical simulation of the subsurface ground deformations due to methane hydrate dissociation. Computers and Geotechnics 34 (4), 216–228.

Klar, A., Soga, K., Ng, M.Y.A., 2010. Coupled deformation–flow analysis for methane hydrate extraction. Geotechnique 60 (10), 765–776.

Kneafsey, T.J., Tomutsa, L., Moridis, L., Seol, Y., Freifeld, B., Taylor, C.E., Gupta, A., 2005. Methane hydrate formation and dissociation in a partially saturated sand—measurements and observations. In: Proceedings of the Fifth International Conference on Gas Hydrates, Tapir Acad., Trondheim, Norway, pp. 213–220.

Masui, A., Haneda, H., Ogata, Y., Aoki, K., 2005. The effect of saturation degree of methane hydrate on the shear strength of synthetic methane hydrate sediments. In: Proceedings of the Fifth International Conference on Gas Hydrates, Tapir Acad., Trondheim, Norway, pp. 657–663.

Miura, N., Yamanouchi, T., Ueyama, K., 1977. Particle-crushing of granular materials under high triaxial stresses. Journal of the Society of Materials Science Japan 26, 815–818.

Miyazaki, K., Masui, A., Sakamoto, Y., Tenma, N., 2010. Effect of confining pressure on triaxial compressive properties of artificial methane hydrate bearing sediments. In: Proceedings of the Offshore Technology Conference, 20721-MS, http://dx.doi.org/10.4043/20721-MS.

Miyazaki, K., Masui, A., Sakamoto, Y., Aoki, K., Tenma, N., Yamaguchi, T., 2011. Triaxial compressive properties of artificial methane-hydrate-bearing sediment. Journal of Geophysical Research 116, B06102. http://dx.doi.org/10.1029/2010JB008049.

Nagakubo, S., 2009. Methane hydrate as a domestic energy resource: Japan's methane hydrate R&D program. Journal of Geography 118 (5), 758–775.

Newland, P.L., Allely, B.H., 1957. Volume changes in drained triaxial tests on granular materials. Geotechnique 7, 17–34.

Otani, J., Mukunoki, T., Obara, Y., 2000. Application of X-ray CT method for characterization of failure in soils. Soils and Foundations 40 (2), 111–118.

Pradhan, T.B.S., 1997. Characteristics of shear band in plane strain compression tests of sands, Deformation and Progressive Failure in Geomechanics - IS-Nagoya'97, pp. 241–246.

Rowe, P.W., 1962. Stress–dilatancy relation for static equilibrium of an assembly of particles in contact. Proceedings of the Royal Society A 269 (1), 500–527.

Sloan, E.D., 1998. Clathrate Hydrate of Natural Gases, 2nd ed. Marcel Dekker, Inc., New York705.

Suzuki, K., Nagao, J., Narita, H., 2006. Observation of gas hydrate production in sediment deposits using scanning electron microscope. In: Proceedings of the Annual Conference of the Japan Geoscience Union, G228-006 (in Japanese).

Tatsuoka, F., Sakamoto, M., Kawamura, T., Fukushima., S., 1986. Strength and deformation characteristics of sand in plane strain compression at extremely low pressures. Soils and Foundations 26 (1), 65–84.

Tatsuoka, F., Nakamura, S., Huang, C., Tani, K., 1990. Strength anisotropy and shear direction in plane strain tests of sand. Soils and Foundations 30 (1), 35–54.

Tejchman, J., Gorski, J., Einav, I., 2012. Effect of grain crushing on shear localization in granular bodies during plane strain compression. International Journal for Numerical and Analytical Methods in Geomechanics 36 (18), 1909–1931.

Tohidi, B., Anderson, R., Clennell, M.B., Burgass, R.W., Biderkab, A.B., 2001. Visual observation of gas-hydrate formation and dissociation in synthetic porous media by means of glass micromodels. Geology 29, 867–870 (doi:10.1130/0091-7613(2001)029 < 0867:VOOGHF > 2.0.CO;2.).

Uchida, S., Soga, K., Yamamoto, K., 2012. Critical state soil constitutive model for methane hydrate soil. Journal of Geophysical Research 117 (B03209), 13. http://dx.doi.org/10.1029/2011JB008661.

Ueno, K., Takashima, S., Mochizuki, A., 2000. Simple measurement of displacement field of sand by image processing. Journal of JSCE: (III) Geotechnical Engineering 666 (53), 339–344 (in Japanese).

Waite, W.F., Winters, W.J., Mason, D.H., 2004. Methane hydrate formation in partially water-saturated Ottawa sand. American Mineralogist 89, 1202–1207.

Waite, W.F., Santamarina, J.C., Cortes, D.D., Dugan, B., Espinoza, D.N., Germaine, J., Jang, J., Jung, J.W., Kneafsey, T.J., Shin, H., Soga, K., Winters, W.J., Yun, T.-S., 2009. Physical properties of hydrate-bearing sediments. Reviews of Geophysics 47, RG4003. http://dx.doi.org/10.1029/2008RG000279.

White, D.J., Take, W.A., Bolton, M.D., 2003. Soil deformation measurement using particle image velocimetry (PIV) and photogrammetry. Géotechnique 53 (7), 619–631.

Yamamoto, K., 2009. Production techniques for methane hydrate resources and field test programs. Journal of Geography 118 (5), 913–934 (in Japanese).

Yoneda, J., Hyodo, M., Nakata, Y., Yoshimoto, N., 2010. Triaxial shear characteristics of methane hydrate-bearing sediment in the deep seabed.

Journal of JSCE (III): Geotechnical Engineering 66 (4), 742–756 (in Japanese).

Yoneda, J., Hyodo, M., Nakata, Y., Yoshimoto, N., Orense, R.P., 2011. Deformation of seabed due to exploitation of methane hydrate reservoir. Frontiers in Offshore Geotechnics II, Taylor & Francis Group, London, 245–250. http://dx.doi.org/10.1201/b10132-18.

Yoshida, T., Tatsuoka, F., Sidiqquee, M.S.A., Kamegai, Y., Park, C.S., 1994. Shear banding in sands observed in plane strain compression. In: Chambon, R., Desrues, J., Vardoulakis, I. (Eds.), Localization and Bifurcation Theory for Soils and Rocks. Balkema, Rotterdam, pp. 165–179.

Yun, T.S., Francisca, F.M., Santamarina, J.C., Ruppel, C., 2005. Compressional and shear wave velocities in uncemented sediment containing gas hydrate. Geophysical Research Letters 32, L10609. http://dx.doi.org/10.1029/2005GL022607.

Yun, T.S., Santamarina, J.C., Ruppel., C., 2007. Mechanical properties of sand, silt, and clay containing tetrahydrofuran hydrate. Journal of Geophysical Research 112, B04106. http://dx.doi.org/10.1029/2006JB004484.